

输出多线型微环谐振器的研究

张江峰¹, 梁龙学¹, 吴小所^{1,2*}, 吴朝阳^{1,2}, 王嘉伟¹, 孙成龙¹¹兰州交通大学电子与信息工程学院, 甘肃 兰州 730070;²兰州交通大学光电技术与智能控制教育部重点实验室, 甘肃 兰州 730070

摘要 为了能够得到洛伦兹线型、Fano线型、类电磁诱导透明和类电磁诱导吸收这4类线型,提出了一种基于Fabry-Perot(FP)腔的微槽型微环谐振器。该结构在FP腔外侧引入了两个空气孔来提高品质因数。通过改变结构参数和选取不同的波长范围,实现了以上4类线型。采用的模拟仿真方法为时域有限差分法,结合传输矩阵法,对所提结构进行了模拟仿真和参数优化数值模型的建立。仿真结果表明,所提结构的品质因数达到了90112,消光比约为15 dB。

关键词 光学器件; 微环谐振器; 多线型; 微槽型微环; 高品质因数

中图分类号 TN256

文献标志码 A

DOI: 10.3788/AOS221829

1 引言

微环谐振器(MRR)作为一种重要的光学器件,它通常与总线波导进行侧向耦合,总线波导的透射谱中会产生周期性谐振线型,其通常为对称的洛伦兹线型。微环谐振器拥有高品质因子 Q 、紧凑的结构尺寸以及与其他光子器件集成的兼容性,被广泛应用于光互连、非线性光学和传感领域^[1-3]。近年来,Fano线型在这些领域对芯片集成功能的改进^[4-5]引起了人们的广泛关注。与洛伦兹线型相比较,Fano线型具有非对称的特点^[6],Fano共振可传输从0%调谐到100%的波长范围^[7],可以实现光传输强度的剧烈变化。基于Fano线型的这一特点,可以将微环谐振器的谐振线型改变为Fano线型,Fano线型在滤波器^[8-9]、传感器^[10]和全光开关^[11-12]等领域被广泛使用。目前,有多种基于微环谐振器的结构可以实现Fano线型,如多微环谐振器耦合结构^[13]、马赫-增德尔干涉仪(MZI)与微环谐振器耦合结构^[14]等,但是这些结构都不够紧凑。

此外,还可以将微环谐振器的谐振输出线型改变为电磁诱导透明(EIT)和电磁诱导吸收(EIA)线型。EIT现象最早发现于量子系统中^[15],EIT是一种非线性相干光学,它使材料在特定吸收光谱中透明^[16-17]。设备和环境严重限制了EIT在传统原子系统中的应用^[18-19],EIT线型在透明窗口内由于色散特性出现了显著的变化,使得EIT效应在慢光器件、非线性光学、光储存、光开关等领域具有很大的应用优势^[20]。所以,

在结构简单、环境影响不太明显的前提下实现EIT效应仍是一个值得研究的课题。

就EIA而言,它是光与共振光场相互作用表现出来的一种性质,是一种与EIT相对立的实验现象^[21]。EIA的性能使其在高灵敏度传感器、光电调制器、光开关等领域得到广泛应用,因此具有很大的研究价值。

为了得到多线型输出,本文提出了一种基于法布里-珀罗(FP)腔的微槽型微环谐振器,将FP腔的反射信号作为连续态光信号与微环谐振器产生的洛伦兹离散态光信号发生相消干涉,产生Fano线型。同时,在改变结构参数及选取不同波长的情况下还出现了类EIT线型和类EIA线型。该方案通过在FP腔外侧引入两个空气孔,加强光的反射,提高光的利用率和波导与微环的耦合能力,因此在结构简单、紧凑的前提下,该结构的品质因数更高。

2 结构设计与理论推导

2.1 结构设计

基于FP腔的微槽型微环谐振器(FPMGMRR)的立体图如图1(a)所示,微环的半径 $R = 8.88 \mu\text{m}$, W_{slot} 为微槽的宽度。结合文献[22]和结构仿真确定了微环与直波导的耦合距离 L_{gap} 及空气孔的半径 R_{hole} 。 L_0 为FP腔的腔长,将文献[23]中的晶格常数作为FP腔的反射面与外空气孔的距离 L ,波导的宽度 $W_0 = 0.5 \mu\text{m}$, SiO_2 层和Si层的厚度分别为 $3 \mu\text{m}$ 和 220nm 。由图1(b)可以看出,FP腔的反射面及空气孔关于耦合

收稿日期: 2022-10-14; 修回日期: 2022-11-21; 录用日期: 2022-12-06; 网络首发日期: 2023-01-04

基金项目: 国家重点研发计划(2017YFB0504203)、甘肃省自然科学基金(21JR7RA310)、兰州交通大学青年科学基金(2021029)

通信作者: *43452740@qq.com

中心点对称。

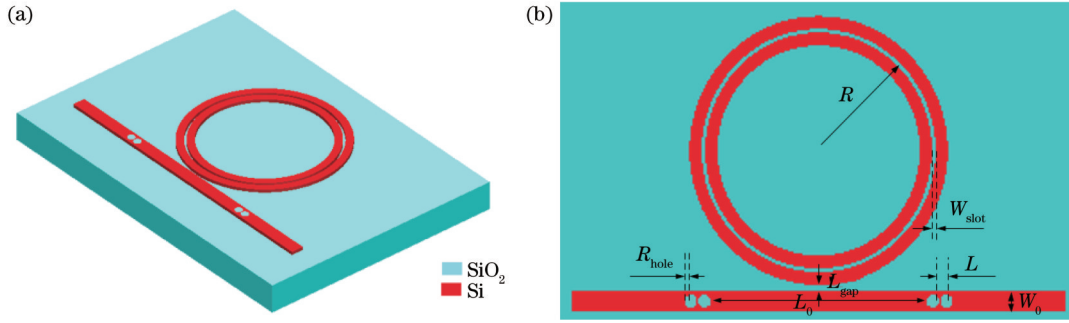


图1 FPMGMRR结构示意图。(a)立体结构示意图;(b)俯视图及相关结构参数

Fig. 1 Structural diagram of FPMGMRR. (a) Diagram of stereo structure; (b) top view and related structure parameters

本次设计采用了微槽型微环与FP腔之间的耦合,使得离散态光模式和连续态光模式在不同波长处发生干涉,从而产生了 Lorentz、Fano、EIT-like、EIA-like 4种线型,Fano效应和EIA-like效应可实现对环境折射率的检测。同时,与传统MRR相比,微槽型微环谐振器可以将大量的光限制在狭缝中,且通过与FP腔的耦合,使得FPMGMRR具有更高的品质因数。

2.2 理论分析

图2为该结构的理论模型,本文采用矩阵传输法对该结构进行理论分析。4个空气孔关于耦合中心对称,且半径均为 R_{hole} 。总线波导具有正向和反向传播的模式,输入和输出模式分别为 a_1, b_2 和 a_2, b_1 ,设孔的反射系数为 r_m ,则孔的传输矩阵为

$$T_m = \frac{1}{i\sqrt{1-r_m^2}} \begin{pmatrix} -1 & -r_m \\ r_m & 1 \end{pmatrix}, \quad (1)$$

式中, $m = 1, 2, 3, 4$ 。

空气孔 h_2 和 h_3 距离波导与MRR的耦合中心的长度分别为 l_2 和 l_3 ,当光在长为 L_0 的FP腔中传播时,传输矩阵为

$$T_{l_2} = \begin{bmatrix} \exp(i2\pi n l_2 / \lambda) & 0 \\ 0 & \exp(-i2\pi n l_2 / \lambda) \end{bmatrix}, \quad (2)$$

$$T_{l_3} = \begin{bmatrix} \exp(i2\pi n l_3 / \lambda) & 0 \\ 0 & \exp(-i2\pi n l_3 / \lambda) \end{bmatrix}, \quad (3)$$

式中: n 为有效折射率; λ 为工作波长。

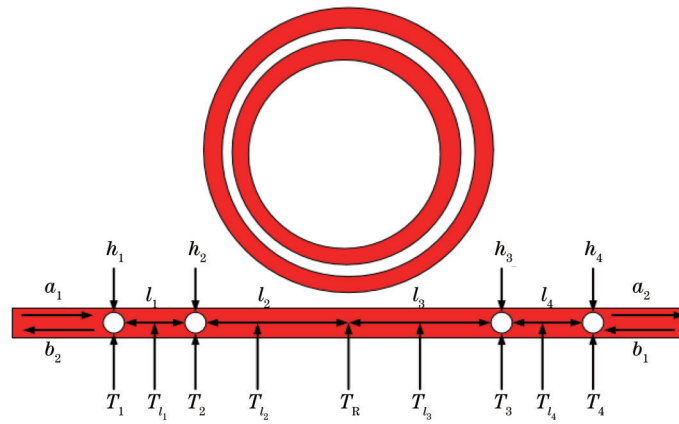


图2 FPMGMRR的理论模型

Fig. 2 Theoretical model of FPMGMRR

当光在空气孔 h_1 和 h_2 以及空气孔 h_3 和 h_4 之间传播时,它们之间也存在光的反射,因此也可以将孔 h_1 与孔 h_2 以及孔 h_3 与孔 h_4 看作是二个FP腔,它们的腔长相等,长度分别为 $l_1 = l_4 = L$,但是它们之间的反射光与微环直接耦合的作用效果可以忽略,因此光在长度为 L 的FP腔中的传输矩阵为

$$T_{l_1} = \begin{bmatrix} \exp(i2\pi n l_1 / \lambda) & 0 \\ 0 & \exp(-i2\pi n l_1 / \lambda) \end{bmatrix}, \quad (4)$$

$$T_{l_4} = \begin{bmatrix} \exp(i2\pi n l_4 / \lambda) & 0 \\ 0 & \exp(-i2\pi n l_4 / \lambda) \end{bmatrix}. \quad (5)$$

当光在MRR中产生谐振时,它的透射谱由

$$t_R(\lambda) = \frac{\tau - a \exp(i2\pi n L_R / \lambda)}{1 - \tau a \exp(i2\pi n L_R / \lambda)}$$

决定, τ 是波导与微环耦合区域中的传输系数, $a = \exp(-\alpha L_R)$ 表示光在微环中的传输系数, α 表示传输损耗系数, L_R 表示微环的周长。光在耦合中心的传输矩阵可以表示为

$$T_R = \begin{bmatrix} t_R & 0 \\ 0 & 1 \end{bmatrix}, \quad (6)$$

$$\begin{bmatrix} b_1 \\ a_2 \end{bmatrix} = T_1 T_{l_1} T_2 T_{l_2} T_R T_{l_3} T_3 T_{l_4} T_4 \begin{bmatrix} a_1 \\ b_2 \end{bmatrix}. \quad (7)$$

则整个耦合系统的传输矩阵为

综上所述,基于FP腔的微槽型微环谐振器的归一化透射率为

$$\left| \frac{a_2}{a_1} \right|^2 = \left| \frac{t_1 t_2 \exp(i2\pi n l_1 / \lambda)}{1 - r_1 r_2 \exp(i4\pi n l_1 / \lambda)} \right|^2 \left| \frac{t_2 t_3 t_R \exp(i2\pi n l / \lambda)}{1 - r_2 r_3 \exp(i4\pi n l / \lambda)} \right|^2 \left| \frac{t_3 t_4 \exp(i2\pi n l_4 / \lambda)}{1 - r_3 r_4 \exp(i4\pi n l_4 / \lambda)} \right|^2, \quad (8)$$

式中: $l = l_2 + l_3$; $t_m (m = 1, 2, 3, 4)$ 为孔的透射系数, 且 $t_m = \sqrt{1 - r_m^2}$; t_R 为耦合中心的透射系数。

3 器件结构选择

目前, 研究人员利用集成光学工艺实现了光电器件的片上集成^[24]。为了实现功能更加强大的光电集成芯片, 器件尺寸会越来越小, 因此器件制造工艺难度越来越大。本文所提结构为基于FP的微槽型微环谐振器。从工艺角度来讲, 与非开槽环形谐振腔相比, 对环形谐振腔进行开槽会大大增加工艺难度。为了使器件的消光比(ER)和品质因子有所改善, 本文选择了微槽型微环谐振器。

图 3 为基于 FP 腔的非开槽微环谐振器(FPNMGMRR), 其余参数与图 1(b)所示完全相同。通过模拟仿真可得, FPMGMRR 的 Q 值为 90112, 而 FPNMGMRR 的 Q 值为 43219.7。图 4 为两个器件的透射光谱, 从图 4 可以看出, FPNMGMRR 的 ER 相对较小。

FPMGMRR 与 FPNMGMRR 的截面模场分布图如图 5 所示, 图中展示了将光限制在微槽和环波导中的两种情形。仿真是在 $\lambda = 1.55 \mu\text{m}$ 时进行的, 仿真结果表明, 图 5(a) 中群折射率 $n_g = 3.24$, 图 5(b) 中 $n_g = 4.34$ 。

自由光谱范围为

$$R_{FS} = \frac{\lambda^2}{2\pi n_g R}. \quad (9)$$

在仿真过程中, FPMGMRR 与 FPNMGMRR 的半径相等。由式(9)可知, FPMGMRR 的自由光谱范

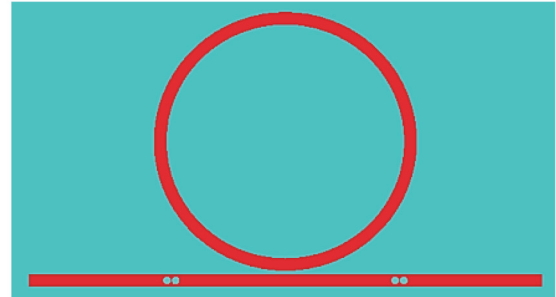


图 3 FPNMGMRR 示意图
Fig. 3 Schematic diagram of FPNMGMRR

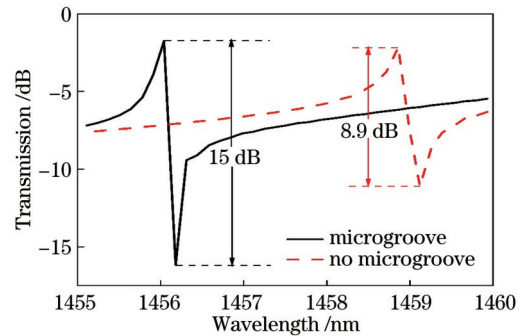


图 4 FPMGMRR 与 FPNMGMRR 的透射光谱
Fig. 4 Transmission spectra of FPMGMRR and FPNMGMRR

围较大。要想增大 R_{FS} , 就得减小微环半径, 这样会使得微环的弯曲损耗增大。所以, 当 FPNMGMRR 与 FPMGMRR 拥有相同的 R_{FS} 时, FPNMGMRR 的弯曲损耗会更大。

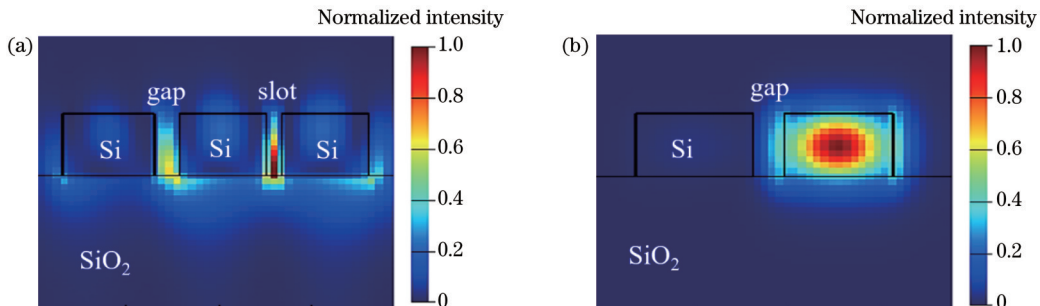


图 5 FPMGMRR 和 FPNMGMRR 的模场分布。(a) FPMGMRR 的模场分布; (b) FPNMGMRR 的模场分布
Fig. 5 Mode field distributions of FPMGMRR and FPNMGMRR. (a) Mode field distribution of FPMGMRR; (b) mode field distribution of FPNMGMRR

4 器件结构仿真与优化

本文通过采用 Lumerical 仿真软件及三维时域有限差分 (3D-FDTD) 方法对该结构进行模拟仿真。通过调节 L_{gap} 的大小来影响耦合系数 k 的大小,通过调节 R_{hole} 的大小来影响 FP 腔的反射系数,通过改变 W_{slot} 与 L 的大小来实现对输出线型的调控。

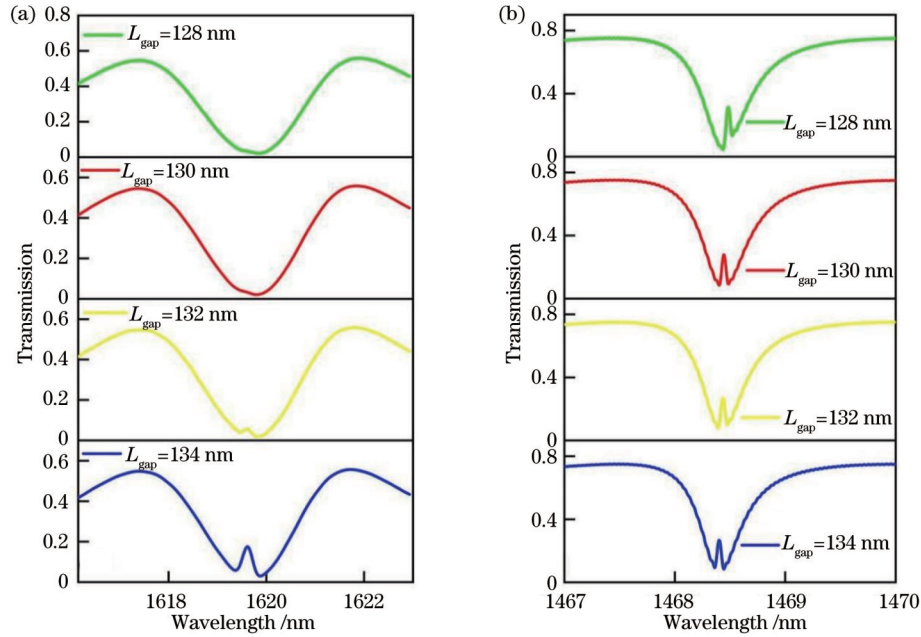


图 6 类 EIT 谱线随 L_{gap} 的变化。(a) $R_{hole} = 0.156 \mu\text{m}, L = 0.455 \mu\text{m}$; (b) $R_{hole} = 0.150 \mu\text{m}, L = 0.335 \mu\text{m}$

Fig. 6 EIT-like spectral lines varying with L_{gap} . (a) $R_{hole} = 0.156 \mu\text{m}, L = 0.455 \mu\text{m}$; (b) $R_{hole} = 0.150 \mu\text{m}, L = 0.335 \mu\text{m}$

当 $R_{hole} = 0.15 \mu\text{m}, L = 0.335 \mu\text{m}$ 时,随着 L_{gap} 的增加,类 EIT 窗口内的谐振峰的位置发生了左移,从 $\lambda = 1468.48 \text{ nm}$ 移动到 $\lambda = 1468.40 \text{ nm}$ 。窗口内谐振峰的强度也有减弱的趋势,其中类 EIT 线型的对称性也发生了变化,在 $L_{gap} = 130 \text{ nm}$ 时的对称性较好。

基于以上优化结果,在选取 $R_{hole} = 0.15 \mu\text{m}, L_{gap} = 130 \text{ nm}$ 的情况下,如图 7 所示,通过调节 FP 反射面与外空气孔之间的距离 L 来改变类 EIT 窗口内谐

4.1 耦合距离与 FP 腔长度

如图 6 (a) 所示,当 $R_{hole} = 0.156 \mu\text{m}, L = 0.455 \mu\text{m}$ 时:当 L_{gap} 为 128 nm 和 130 nm 时,EIT 窗口为关闭状态;当 $L_{gap} = 132 \text{ nm}$ 时,EIT 窗口逐渐打开;当 $L_{gap} = 134 \text{ nm}$ 时, $\lambda = 1619.62 \text{ nm}$ 处出现了较强的谐振峰,产生了类 EIT 现象。

振峰的强度。图 7(b) 为图 7(a) 中虚线框部分的放大图。从图 7(b) 中可以明显看出,随着 L 的增大,EIT 窗口内的谐振峰强度逐渐增大,这是因为:当 L 增大时,孔 h_1 和孔 h_2 以及孔 h_3 与孔 h_4 组成的结构可看作是二个 FP 腔,虽然它们与微环没有形成直接耦合,但是随着腔长的增加,它们提高了光的利用率,增强了空气孔之间光的反射,提高了 FP 腔与微环的耦合能力,从而导致窗口内谐振峰强度的增强,使得类 EIT 现象更加明显。

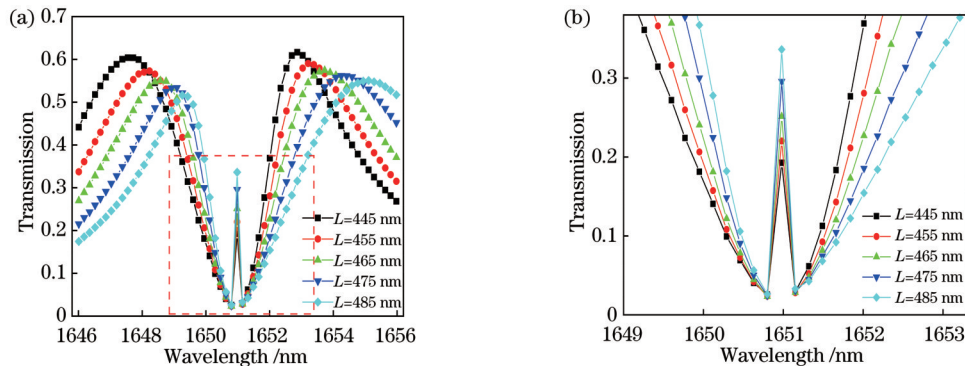


图 7 类 EIT 谱线随 L 的变化。(a) 类 EIT 透光光谱; (b) 图 7(a) 虚线框内曲线的放大图

Fig. 7 EIT-like spectral lines varying with L . (a) EIT-like transmission spectra; (b) amplification of curves in dashed box in Fig. 7(a)

4.2 空气孔半径与微槽宽度

空气孔半径 R_{hole} 对类 EIA 的影响如图 8(a) 所示。随着 R_{hole} 的逐渐增大, 类 EIA 的共振波长的透射率逐渐变大, 而且使得吸收窗口的宽度也逐渐变窄。当空气孔的半径变大时, L 会相对减小, 使得空气孔对光的反射能力减弱, 从而使得 FP 腔与微环的耦合作用减弱, 它们之间的相消干涉也逐渐减弱。在 R_{hole} 增大的

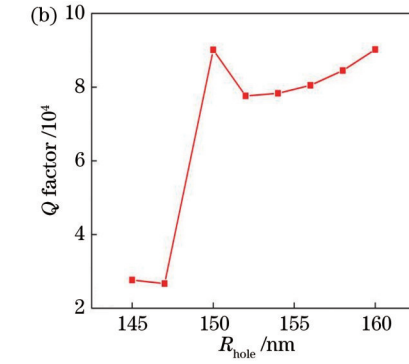
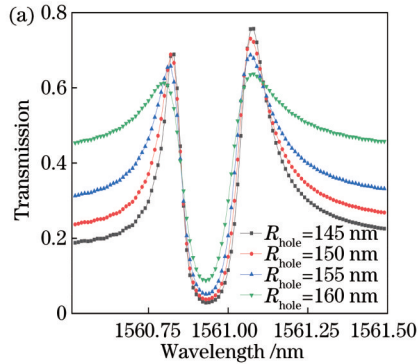


图 8 类 EIA 谱线随 R_{hole} 的变化。(a) 类 EIA 透射光谱; (b) Q 值

Fig. 8 EIA-like spectral lines varying with R_{hole} . (a) EIA-like transmission spectra; (b) Q value

图 9 为微槽宽度 W_{slot} 对类 EIA 线型的影响。随着 W_{slot} 的增大, 类 EIA 线型发生了明显的左移, 吸收窗口内的共振波长从 1568.98 nm 左移至 1561.97 nm。在此过程中, 类 EIA 的透射率也发生了变化, 所以实现了 W_{slot} 对透射谱的调制。从图 9 中可以看出, 吸收窗口内的透射率逐渐向 0 趋近, 这是因为随着 W_{slot} 的逐渐增大, 微槽对光的限制能力减弱。当传输效率为 0 时, 可以认为窗口处于关闭状态, 因而可以将 EIA 的这种特性广泛应用于光开关领域。

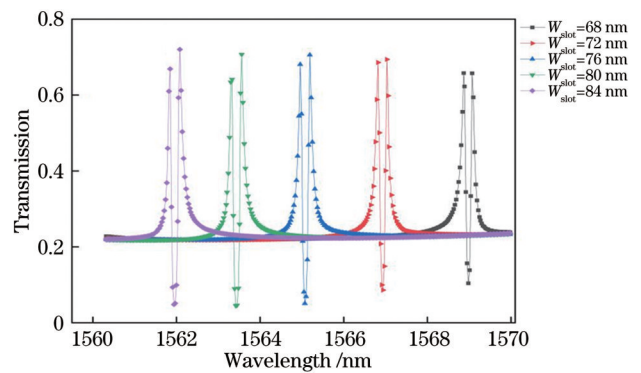


图 9 类 EIA 谱线随 W_{slot} 的变化

Fig. 9 EIA-like spectral lines varying with W_{slot}

目前, 硅基材料的纳米级制造工艺仍有很大的提升空间^[25]。但是, 在一些结构复杂、尺寸为纳米级的结构的制造过程中可能会产生一定的误差, 导致实现的结果与预期结果有一定的偏差。为了保证结构的可实现性, 本文在实现最优输出线型的前提下, 分析了耦合距离 L_{gap} 和空气孔距离 L 在 ± 10 nm 的范围内波动时

过程中, 可以看作 FP 腔与微环逐渐远离了临界耦合状态, 因为在临界耦合状态时 EIA 谱线的最小值是趋于 0 的。此外, 还研究了 R_{hole} 对 Q 值的影响。如图 8(b) 所示, 当 R_{hole} 从 147 nm 增加到 150 nm 的过程中, Q 值迅速增加, 在此之后, Q 值又减小, 当 R_{hole} 从 152 nm 增加到 160 nm 的过程中, Q 值又缓慢地增加。其中 Q 值的最大值为 150 nm 处的 90112。

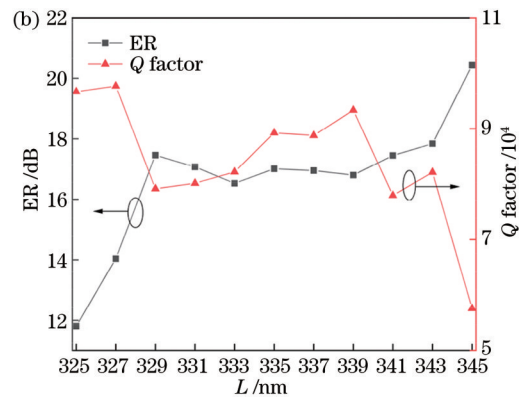
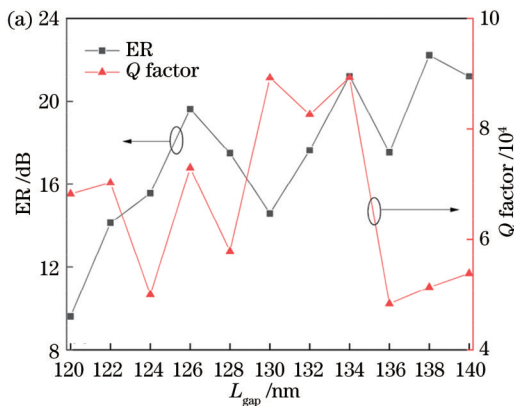


图 10 L_{gap} 和 L 对品质因数 Q 和 ER 的影响。(a) L_{gap} ; (b) L

Fig. 10 Influences of L_{gap} and L on quality factor Q and ER. (a) L_{gap} ; (b) L

在 325~345 nm 之间波动时,最低的 Q 值达到了 57598,除了 $L=325$ nm 外,ER 的最小值在 14 dB 以上。而且,在 329~343 nm 之间, Q 值在 77993.3 与 93338.6 之间波动,ER 在 16.53 dB 与 17.84 dB 之间波动,表现出较好的稳定性。图 10 的结果表明,本文所提结构具有较好的工艺容差性。

5 结 论

提出了一种基于 FP 腔的微槽型微环谐振器,在 FP 腔外引入了两个空气孔,以提高光的利用率、增强 FP 腔与微环的耦合作用。首先使用传输矩阵法对该结构进行了理论分析,然后通过 Lumerical 仿真软件仿真了耦合距离、FP 腔的长度、空气孔半径及微槽宽度对类 EIT 和类 EIA 线型的影响。通过仿真分析,最终实现了洛伦兹、Fano、类 EIT、类 EIA 4 种线型,而且该结构的 Q 值达到了 90112,ER 约为 15 dB。该结构具有尺寸小、结构简单紧凑和可实现性强等优点,可用于光开关等领域。

参 考 文 献

- [1] Jang J K, Klenner A, Ji X C, et al. Synchronization of coupled optical microresonators[J]. *Nature Photonics*, 2018, 12(11): 688-693.
- [2] Kippenberg T J, Holzwarth R, Diddams S A. Microresonator-based optical frequency combs[J]. *Science*, 2011, 332(6029): 555-559.
- [3] Zhang W W, Serna S, Le Roux X, et al. Highly sensitive refractive index sensing by fast detuning the critical coupling condition of slot waveguide ring resonators[J]. *Optics Letters*, 2016, 41(3): 532-535.
- [4] Hu T, Yu P, Qiu C, et al. Tunable Fano resonances based on two-beam interference in microring resonator[J]. *Applied Physics Letters*, 2013, 102(1): 011112.
- [5] Zhao G L, Zhao T, Xiao H F, et al. Tunable Fano resonances based on microring resonator with feedback coupled waveguide[J]. *Optics Express*, 2016, 24(18): 20187-20195.
- [6] 廖莎莎, 包航, 张甜甜, 等. 基于光栅辅助微环结构的高斜率 Fano 谐振器[J]. *光学学报*, 2021, 41(22): 2213001.
Liao S S, Bao H, Zhang T T, et al. High-slope Fano resonator based on grating-assisted microring structure[J]. *Acta Optica Sinica*, 2021, 41(22): 2213001.
- [7] Fan S H. Sharp asymmetric line shapes in side-coupled waveguide-cavity systems[J]. *Applied Physics Letters*, 2002, 80(6): 908-910.
- [8] Zhou L J, Poon A W. Electrically reconfigurable silicon microring resonator-based filter with waveguide-coupled feedback[J]. *Optics Express*, 2007, 15(15): 9194-9204.
- [9] Zhao Y H, Wang X, Gao D S, et al. On-chip programmable pulse processor employing cascaded MZI-MRR structure[J]. *Frontiers of Optoelectronics*, 2019, 12(2): 148-156.
- [10] Zhou X Y, Zhang L, Armani A M, et al. On-chip biological and chemical sensing with reversed fano lineshape enabled by embedded microring resonators[J]. *IEEE Journal of Selected Topics in Quantum Electronics*, 2014, 20(3): 35-44.
- [11] Wu J H, Gao J Y, Xu J H, et al. Ultrafast all optical switching via tunable Fano interference[J]. *Physical Review Letters*, 2005, 95(5): 057401.
- [12] Yao Y H, Cheng Z, Dong J J, et al. Performance of integrated optical switches based on 2D materials and beyond[J]. *Frontiers of Optoelectronics*, 2020, 13(2): 129-138.
- [13] Zhou X Y, Zhang L, Armani A M, et al. An integrated photonic gas sensor enhanced by optimized fano effects in coupled microring resonators with an athermal waveguide[J]. *Journal of Lightwave Technology*, 2015, 33(22): 4521-4530.
- [14] 李欣. 新型微环谐振器及其传感特性研究[D]. 哈尔滨: 哈尔滨工业大学, 2015: 83-87.
Li X. Novel microring resonators and sensing properties[D]. Harbin: Harbin Institute of Technology, 2015: 83-87.
- [15] 王子煜, 邵健, 胡亚新, 等. 基于全介质超材料的高 Q 电磁诱导透明现象研究[J]. *光学学报*, 2021, 41(11): 1116001.
Wang Z Y, Shao J, Hu Y X, et al. Electromagnetically induced transparency based on all-dielectric metamaterial with high Q factor[J]. *Acta Optica Sinica*, 2021, 41(11): 1116001.
- [16] Liu Y C, Li B B, Xiao Y F. Electromagnetically induced transparency in optical microcavities[J]. *Nanophotonics*, 2017, 6(5): 789-811.
- [17] Lu X Q, Shi J H, Liu R, et al. Highly-dispersive electromagnetic induced transparency in planar symmetric metamaterials[J]. *Optics Express*, 2012, 20(16): 17581-17590.
- [18] Dong Z W, Sun C, Si J N, et al. Tunable polarization-independent plasmonically induced transparency based on metal-graphene metasurface[J]. *Optics Express*, 2017, 25(11): 12251-12259.
- [19] Yang M S, Liang L J, Zhang Z, et al. Electromagnetically induced transparency-like metamaterials for detection of lung cancer cells[J]. *Optics Express*, 2019, 27(14): 19520-19529.
- [20] 蒋藩. 基于光子晶体纳米梁腔的类电磁诱导透明和吸收效应研究[D]. 湘潭: 湘潭大学, 2020: 3-6.
Jiang F. Study on electromagnetically induced transparency and absorption effects based on photonic crystal nanobeam cavity[D]. Xiangtan: Xiangtan University, 2020: 3-6.
- [21] 杨广玉, 陈良超, 米成栋, 等. 玻色爱因斯坦凝聚体中电磁诱导透明和电磁诱导吸收的研究[J]. *量子光学学报*, 2018, 24(2): 156-163.
Yang G Y, Chen L C, Mi C D, et al. Electromagnetically induced transparency and electromagnetically induced absorption in ^{87}Rb Bose-Einstein condensate[J]. *Journal of Quantum Optics*, 2018, 24(2): 156-163.
- [22] Gu L P, Fang L, Fang H L, et al. Fano resonance lineshapes in a waveguide-microring structure enabled by an air-hole[J]. *APL Photonics*, 2020, 5(1): 016108.
- [23] Peng F C, Wang Z R, Yuan G H, et al. High-sensitivity refractive index sensing based on Fano resonances in a photonic crystal cavity-coupled microring resonator[J]. *IEEE Photonics Journal*, 2018, 10(2): 6600808.
- [24] 孙道鑫, 张东亮, 毕付, 等. 应用于集成光学陀螺敏感单元的硅基微环谐振腔[J]. *激光与光电子学进展*, 2022, 59(13): 1313001.
Sun D X, Zhang D L, Bi F, et al. Silicon-based microring resonant cavity applied to integrated optical gyroscope sensitive unit[J]. *Laser & Optoelectronics Progress*, 2022, 59(13): 1313001.
- [25] 刘春娟, 桑常林, 吴小所, 等. 一维光子晶体槽型微环谐振器及其传感特性[J]. *光学学报*, 2020, 40(24): 2413002.
Liu C J, Sang C L, Wu X S, et al. One-dimensional photonic crystal groove microring resonators and its sensing characteristics[J]. *Acta Optica Sinica*, 2020, 40(24): 2413002.

Research on Output Multiline Microring Resonator

Zhang Jiangfeng¹, Liang Longxue¹, Wu Xiaosuo^{1,2*}, Wu Chaoyang^{1,2}, Wang Jiawei¹,
Sun Chenglong¹

¹*School of Electronics and Information Engineering, Lanzhou Jiaotong University, Lanzhou 730070, Gansu, China;*

²*Key Laboratory of Opto-Technology and Intelligent Control, Ministry of Education, Lanzhou Jiaotong University, Lanzhou 730070, Gansu, China*

Abstract

Objective In order to achieve electromagnetically induced transparency (EIT) in the quantum field, it is necessary to meet harsh experimental conditions such as extremely low experimental temperatures, high-intensity light sources, and huge experimental equipment. Therefore, the development of EIT is greatly limited. With the development of photonics, the realization of EIT in the field of photonics will avoid harsh experimental conditions and accelerate the research on EIT. The electromagnetically induced absorption (EIA) effect is contrary to EIT. The physical mechanism of EIA is radiation and sub-radiation resonator, which realizes EIA through the near-field coupling between them. The EIA effect can be used in the fields of optical switches and slow light devices. In addition, compared with Lorentz linetype, Fano linetype has the characteristics of asymmetry, and the transmission efficiency of the Fano effect is higher. In view of the difficulty in realizing the EIT effect in the quantum field, the application scope of the EIA effect, and the transmission advantages of the Fano effect, the feasibility of these physical effects in a simple and compact device is worthy of studying.

Methods Two main research methods are used in this study, namely the transmission matrix method and the finite difference time domain (FDTD) method. The transmission matrix method is used to analyze the transmission characteristics of devices. Specifically, the transmission matrixes of the air hole, Fabry-Perot (FP) cavity, and coupling between the microring and the FP cavity are established using the parameters such as the reflection coefficient of the air hole, the length of the FP cavity, the wavelength, the effective refractive index, the circumference of the microring, and the transmission loss coefficient. Through the relationship between these matrices, the input mode and the output mode in the waveguide are connected. By analyzing the input and output modes, the expression of normalized transmittance is obtained. The device is simulated by FDTD. It mainly simulates the mode field, transmission spectrum, and performance parameters [quality factor and extinction ratio (ER)] of a microring resonator (MRR). The mode field is simulated at the wavelength of 1550 nm. According to Eq. (9) and the group refractive index in the simulation results, the bending losses of microgroove microring and single waveguide microring are compared. The simulation of the transmission spectrum is mainly shown in the device structure simulation and optimization module. By changing the structural parameters, such as the coupling distance, the length of the FP cavity, the radius of the air hole, and the width of the microgroove, the optimal output linetype can be ensured.

Results and Discussions In this study, the coupling structure of the FP cavity and microgroove microring is adopted (Fig. 1), which makes the light mode of continuous state in the FP cavity and that of discrete state in the microring couple interfere with each other. In addition, the waveform is distorted by the high refractive index difference of the straight waveguide and the FP cavity, and Lorentz linetype, Fano linetype, EIT-like linetype, and EIA-like linetype appear between two adjacent resonance peaks of the FP cavity. In order to improve the utilization of light, reduce the loss, and improve the quality factor of the device, two air holes are introduced outside the FP cavity, and the microgroove structure is adopted. The microgroove structure restricts light. When the distance between the external air hole and the FP cavity increases, the cavity length (L) of the FP cavity of the reflector composed of the air hole increases. In this process, it can be seen from Eq. (8) that the transmissivity of the structure mentioned in this study increases. This phenomenon can be clearly seen in Fig. 7. With the increase in L , the resonance intensity in the EIT transparent window gradually increases. When the radius (R_{hole}) of the air hole increases, L will decrease relatively. In this process, it can be seen from Eq. (8) that the transmissivity of the device will gradually decrease, and this process is consistent with the results shown in [Fig. 8(a)]. Fig. 8(b) also shows that when R_{hole} increases, the quality factor slowly decreases.

Conclusions In this study, a microgroove MRR based on the FP cavity is proposed. Two air holes are introduced outside the FP cavity. By adding air holes, the utilization of light is improved, the coupling ability between the FP cavity and the microring is enhanced, and the transmissivity of the device is improved. FDTD is used to simulate the effects of

coupling distance, FP cavity length, air hole radius, and micro slot width on the output linetype of the device. The results show that: the coupling distance can directly control the EIT-like linetype, and the EIT transparent window can be opened and closed by changing the coupling distance; the length of the FP cavity and the radius of the air hole determine the utilization of light; the width of the microgroove can realize the regulation of EIA. In addition, this study also compares the advantages and disadvantages of single waveguide microring and microgroove microring. The fabrication of single waveguide microring is simple, but the bending loss of microgroove microring is small. In order to simulate the realizability of the device, the fabrication tolerance of the device is simulated on the premise of ensuring the optimal output linetype. The results show that the proposed device has favorable fabrication tolerance and strong realizability. Through the simulation analysis, the multiline output is realized; the Q value of the structure reaches 90112, and the ER is about 15 dB. The proposed structure can be used in the field of optical switches.

Key words optical devices; microring resonator; multiline; microgroove microring; high quality factor